RESEARCH   **Open Access**

Check for updates

Structural, Optical and Photocatalytic Activity of Multi-heterojunction Bi_2O_3/$Bi_2O_2CO_3$/$(BiO)_4CO_3(OH)_2$ Nanoflakes Synthesized via Submerged DC Electrical Discharge in Urea Solution

E. Hashemi, R. Poursalehi[*] and H. Delavari

Abstract

In this research, a novel ternary multi-heterojunction Bi_2O_3/$Bi_2O_2CO_3$/$(BiO)_4CO_3(OH)_2$ photocatalyst is fabricated via submerged DC electrical arc discharge in urea solution. FT-IR, XRD, EDS and PL results confirm the formation of Bi_2O_3/$Bi_2O_2CO_3$/$(BiO)_4CO_3(OH)_2$ multi-heterojunction. Formation of nanoflake morphology is revealed by FE-SEM and TEM images. The optical properties and intense absorption edge of Bi_2O_3/$Bi_2O_2CO_3$/$(BiO)_4CO_3(OH)_2$ reveal the proper visible light absorbing ability. The photocatalytic performance of the sample is investigated via the degradation of methylene orange (MeO) and rhodamine B (RB) under visible light irradiation. The photocatalytic activity of Bi_2O_3/$Bi_2O_2CO_3$/$(BiO)_4CO_3(OH)_2$ is compared with the synthesized sample in water, Bi_2O_3/Bi/$Bi(OH)_3$, which exhibits much higher photocatalytic activity. Also, the stable photodegradation efficiency of Bi_2O_3/$Bi_2O_2CO_3$/$(BiO)_4CO_3(OH)_2$ after four cycles reveals the long-term stability and reusability of the synthesized photocatalyst. The PL intensity of Bi_2O_3/$Bi_2O_2CO_3$/$(BiO)_4CO_3(OH)_2$ shows an improved separation rate of electron–hole pairs and so enhanced photocatalytic performance. The improved photocatalytic activity can be ascribed to the formation of multi-heterojunctions, flake morphology and intrinsic internal electric field (IEF). Multi-heterojunction nanoflakes enhance the absorbance of visible light and facilitate the separation and transport of photogenerated electron holes through large IEF. Our work offers an effective method for the production of innovative bismuth-based photocatalyst with excellent prospects for the degradation of environmental pollutants and light harvesting for renewable energy generation under visible light.

Keywords: Bi_2O_3/$Bi_2O_2CO_3$/$(BiO)_4CO_3(OH)_2$ nanoflakes, Multi-heterojunction, Photocatalyst, Optical properties, Submerged DC electrical discharge, Urea solution

Introduction

Energy crisis and environmental pollution are one of the major global problems in the present century [1]. Hence, semiconductor photocatalysts have attracted great attention in this matter. Photocatalysis with solar energy is one of the most advanced and encouraging techniques in reducing energy crisis and environmental pollution [1–2, 3, 4]. The light of the sun as an inexhaustible energy source is used for the removal of environmental pollutants as well as water splitting and CO_2 photoreduction to generate hydrogen and carbon-containing fuels to overcome energy scarcity [5–6, 7, 8]. So, the synthesis of efficient photocatalysts with high performance in absorbing visible light and charge separation as well as photochemical stability is a key challenge [9]. For example,

*Correspondence: poursalehi@modares.ac.ir

Department of Materials Engineering, Tarbiat Modares University, Tehran 14115-143, Iran

Hashemi *et al. Nanoscale Research Letters*   (2022) 17:75

Page 2 of 16

three-dimensional hierarchical $CuCo_2S_4$ microspheres with considerable photocatalytic activity in removing tetracycline hydrochloride. The high photocatalytic activity is related to the high charge separation efficiency as well as the large specific surface area [10]. Visible-light-driven photocatalysts with heterojunctions have found much attention in the degradation of a wide range of toxic compounds, especially hazardous dyes in wastewater [11, 12]. The photocatalytic activity depends not only on the material but also on the dimensions and structure as well as the composition of the photocatalysts [13, 14]. Bismuth-based complex oxide semiconductors are new promising materials for environmental remediation, water splitting and photocatalytic applications, which show a good photocatalytic performance under visible light [15].Among the diverse photocatalytic materials such as TiO_2, ZnO, SnO_2, WO_3 and CeO_2, bismuth-based photocatalysts are an important group with low toxicity compared to other photocatalysts which have photocatalytic performance for the degradation of organic pollutants in the environment as well as industrial hazardous wastes [16, 17]. In the electronic structure of bismuth oxide, the valence band consists of O 2*p* and Bi 6*s* hybrid orbitals. The Bi 6*s* orbital raises the mobility of photogenerated charge carriers and thus leads to a decrease in the band gap [15, 18]. Bi_2O_3 is a p-type semiconductor which has a direct band gap energy of less than 3.0 eV [19]. There are six main polymorphs for Bi_2O_3, which crystallize into different crystal structures [20]. The monoclinic α-Bi_2O_3 phase is the most stable phase at room temperature [21]. Thermodynamically, α-Bi_2O_3 is stable between 25 and 730 °C and then transformed to face-centered cubic δ-Bi_2O_3 phase at 730 °C and remains stable up to its melting point at 825 °C [20, 22]. The tetragonal β-Bi_2O_3 and body-centered cubic γ-Bi_2O_3 are metastable phases, which are formed at high temperatures and can stabilize down to room temperature or transform to α-Bi_2O_3 at high cooling rates [23, 24]. In addition, thermal transformation of α-Bi_2O_3 and β-Bi_2O_3 to $Bi_2O_2CO_3$ and $(BiO)_4CO_3(OH)_2$ was reported previously [25, 26]. Bismuth oxides, including α-Bi_2O_3, β-Bi_2O_3, γ-Bi_2O_3 and δ-Bi_2O_3, as well as $Bi_2O_2CO_3$ and $(BiO)_4CO_3(OH)_2$ show photocatalytic activity [20, 23–, 26, 27, 28, 29]. However, the small specific surface area, chemical instability and high recombination rate of photogenerated carriers of Bi_2O_3 demonstrate the main problem for applications of Bi_2O_3 as a photocatalyst merely [15]. Several approaches are developed to overcome the drawbacks of using a single-phase semiconductor as a photocatalyst, namely metal or ion doping, establishing composites or formation of multi-junctions [21–, 30, 31, 32]. Among them, the formation of multi-junctions has gained a lot of attention and has been used widely [32]. The construction of a

heterojunction can efficiently improve photocatalytic activity by increasing the separation of photogenerated electrons and holes effectively, for example, 0D/2D S-scheme N-CDs/S-C_3N_4 heterojunction with excellent photocatalytic activity in degradation of organic pollutants and H_2 evolution. The improved photocatalytic performance was attributed to the formation of S-scheme heterojunction with high redox potentials between nitrogen-doped carbon dots (N-CDs) and sulfur-doped carbon nitride (S-C_3N_4) semiconductor [33]. In addition, multi-heterojunctions can show better charge transport mechanism and thus higher photocatalytic activity. As an example of a heterogeneous photocatalytic reaction with efficient carrier separation and well-matched energy band structure, can refer to the organic/inorganic PDI-Urea/BiOBr S-scheme heterojunction with photocatalytic performance for the degradation of antibiotics such as ofloxacin, tetracycline as well as high–low junction OV-BiOBr/$Cu_{2-x}S$ with double defects namely, oxygen and copper vacancy for hydrogen evolution [34, 35]. In addition to these, we can refer to visible light photoresponse AgI-loaded BiOI, Bi_2S_3/Bi_2O_3/$Bi_2O_2CO_3$ ternary nanocomposites, Z-scheme Ag–AgI/BiOI–Bi_2O_3 photocatalysts and SnO_2/Bi_2O_3/BiOI nanofibers with enhanced photocatalytic performance [36–, 37, 38, 39]. IEF is a factor in improving photocatalytic activity by means of simplifying transformation and separation of the photogenerated carriers. The alternative layer structure of $(Bi_2O_2)^{2+}$ fluorite flake and $(MO_6)^{2-}$ perovskite layers in bismuth-based binary metal oxides form IEF that enhanced the separation efficiency of photogenerated charge carriers [26, 40]. Bismuth subcarbonate with $Bi_2O_2CO_3$ chemical formula is an n-type photocatalyst and has shown photocatalytic performance in the decomposition of pollutants in wastewater and polluted air [15, 41, 42]. The electronic structure of $Bi_2O_2CO_3$ is composed of hybridized O 2*p* and Bi 6*p* orbitals in the conduction band and O 2*p*, Bi 6*p* and C 2*p* orbitals in the valence band [15]. The structure of $Bi_2O_2CO_3$ is composed of$(Bi_2O_2)^{2+}$ slabs that are intertwined by means of CO_3^{2-} layers, which lead to a large IEF and improved photocatalytic performance [26, 43]. However, the photocatalytic application of $Bi_2O_2CO_3$ under the solar spectrum is limited due to the wide band gap between 2.8 and 3.5 eV and low charge separation efficiency [26, 43, 44]. Hence, the formation of junctions between $Bi_2O_2CO_3$ and other visible responsive photocatalytic semiconductors like α-Bi_2O_3 is an appropriate way to extend the photocatalytic activity even under visible light, such as α-Bi_2O_3/$Bi_2O_2CO_3$ and $Bi_2O_2CO_3$/Bi_2S_3, $Bi_2O_2CO_3$/BiOCl [44, 45, 46]. $(BiO)_4CO_3(OH)_2$ as an Aurivillius oxide with 2.17 eV band gap is a promising visible-light driven photocatalyst [26]. $(BiO)_4CO_3(OH)_2$ has the same

Hashemi *et al. Nanoscale Research Letters* (2022) 17:75

Page 3 of 16

structure as $Bi_2O_2CO_3$ and can be formed by replacing CO_3^{2-} layers of $Bi_2O_2CO_3$ with OH^- layers which are more polar and increase IEF of photocatalyst and thus lead to more photocatalytic performance [26, 47]. Therefore, $Bi_2O_2CO_3$ and $(BiO)_4CO_3(OH)_2$ are suitable candidates for construction of layered nanostructures with a large IEF and a high ability to separate photogenerated carriers [26, 43]. Consequently, the formation of junctions between $(BiO)_4CO_3(OH)_2$ and $Bi_2O_2CO_3$ can improve visible light photocatalysis activity [26, 48]. The interfaces between $(BiO)_4CO_3(OH)_2$ and $Bi_2O_2CO_3$, which are nearly contacted and have an efficient built-in electric field, improve the separation of photogenerated carriers and lead to better photocatalytic performance. $(BiO)_4CO_3(OH)_2/Bi_2O_2CO_3$ with internal polarized heterojunction was synthesized and shows enhanced photocatalytic activity due to the synergetic effect between IEF and carriers separation and indicated great potential in the application for wastewater treatment [26]. There are many growing numbers of methods for the preparation of single-phase or multi-heterojunctions of bismuth-oxide-based nanostructures. Hydrothermal synthesis of α-Bi_2O_3 photocatalysts with nanosheet structure, Bi/Bi_2O_3 nanoparticles' synthesis by Nd:YAG laser ablation, solvothermal preparation of Bi/$Bi_2O_2CO_3$ heterojunction photocatalyst, synthesis of photocatalytic dendritic α-$Bi_2O_3/Bi_2O_2CO_3$ heterostructures with facile transformation, two-dimensional $(BiO)_4CO_3(OH)_2/Bi_2O_2CO_3$ heterostructure photocatalyst formation by in situ photosynthesis and flowerlike Au/$Bi_2O_2CO_3/Bi_2O_3$ multi-heterojunction photocatalysts preparation by one-pot in situ growth, which are reported elsewhere [26, 43–, 49, 50, 51, 52]. Compared with several conventional techniques for nanostructures synthesis, DC electrical arc discharge in liquid provides a straightforward, flexible and cost-effective method for mass production of nanomaterials without environmental footprints [53, 54]. There are some experimental parameters including electrical current, composition of electrodes and the chemical nature of the liquid environment, which impress arc discharge process, as well as nanomaterials formation both during and after synthesis in liquid [55, 56]. The chemical nature of the liquid environment is a determining factor in the final composition of synthesized nanomaterials through electrical arc discharge, for instance, TiC nanoparticles synthesis via electrical arc discharge in organic liquids [57, 58]. Furthermore, Bi/Bi_2O_3 rodlike nanostructures were prepared via oriented aggregation of bismuth-based nanoparticles synthesized by DC arc discharge in water, where water acts as both a synthesis medium and oxidative environment [53].

In this research, novel $Bi_2O_3/Bi_2O_2CO_3/(BiO)_4CO_3(OH)_2$ multi-heterojunction nanoflakes with considerable photocatalytic performance have been synthesized via DC electrical arc discharge in urea solution for the first time. By applying an appropriate DC current between bismuth electrodes, electrical arc discharge causes plasma generation in the solution and forms $Bi_2O_3/Bi_2O_2CO_3/(BiO)_4CO_3(OH)_2$ nanoflakes. This compound exhibits enhanced photocatalytic performance towards degradations of MeO when compared with both single phases α-Bi_2O_3, $Bi_2O_2CO_3$ and $(BiO)_4CO_3(OH)_2$ compounds based on previous studies and synthesized $Bi_2O_3/Bi/Bi(OH)_3$ by arc discharge in water. The photoactivity enhancement can be attributed to the formation of multi-heterojunction nanoflake morphology and improved IEF in $Bi_2O_3/Bi_2O_2CO_3/(BiO)_4CO_3(OH)_2$ nanostructure. To the best of our knowledge, no research has been conducted around the investigation of photocatalytic performance of synthesized ternary $Bi_2O_3/Bi_2O_2CO_3/(BiO)_4CO_3(OH)_2$ nanocomposite by electrical arc discharge in liquid with an efficient photocatalytic activity under visible light for energy and environmental application.

Experimental

Multi-heterojunction $Bi_2O_3/Bi_2O_2CO_3/(BiO)_4CO_3(OH)_2$ and $Bi_2O_3/Bi/Bi(OH)_3$ nanoflakes were synthesized by facile DC electrical arc discharge method in liquid [53, 54]. The synthesis part of nanostructures comprises of a heat-resistant glass container filled with urea in water solution with a concentration of 10 g/L for the synthesis of $Bi_2O_3/Bi_2O_2CO_3/(BiO)_4CO_3(OH)_2$ and deionized water for the synthesis of $Bi_2O_3/Bi/Bi(OH)_3$. The urea was Merck with more than 99% purity. Two 99.9% purity bismuth electrodes were placed in front of each other in vertical mode: One electrode was held fixed, while the other one was movable to make electrodes close to each other in both experiments. The diameter and length of both electrodes were about 5 mm and 30 mm, respectively. The synthesis parts were connected to ARC 200 DC power supply, and a 40A DC current was applied to synthesis of nanostructures. The synthesis process begins by bringing electrodes close together. When electrodes were brought into contact, electrical arc discharge was generated and nanostructures formed. Each discharge lasted about 1–2 s and emitted a very shiny blue light. By establishing electrical discharge, the surface of electrodes was eroded through evaporation and sputtering, and then bismuth atoms and clusters were formed and dispersed in the solution at so lower temperature than the arc hot zone [54, 58, 59]. The suspension of dark nanostructures was formed through synthesis, and the color of suspension became lighter as time passed due to the oxidation of nanostructures.

FTIR spectroscopy was used to determine the functional groups on the surface of the samples. FTIR spectra

Hashemi *et al. Nanoscale Research Letters* (2022) 17:75

Page 4 of 16

were conducted by a PerkinElmer spectrometer on samples using standard KBr pellets. To investigate the crystallographic and phase characteristics of the samples, the powder specimen was analyzed by X'Pert MPD system with Co Kα radiation at 1.78897 Å wavelength. To identify the microstructure, chemical composition, morphology and size distribution of nanostructures, a MIRA TESCAN field emission scanning electron microscope (FE-SEM) with energy-dispersive X-ray spectroscopy (EDS) and elemental mapping of nanostructures as well as a Zeiss EM900 transmission electron microscope (TEM) were used at room temperature. The optical properties of colloidal samples were determined by SCO-TECH SP UV-26 UV–visible spectrophotometer at wavelengths between 190 and 1100 nm at different times. To investigate the photocatalytic activity of synthesized samples, the powder specimen was carried out from solution by using a KTS 5000 rpm centrifuge. PL spectra were recorded by an AvaSpec-2048Tech spectrofluorophotometer, where a Nd:YAG laser with 3rd harmonic crystal was used for excitation of the samples at a wavelength of 355 nm.

The MeO and RB were used as the model pollutants to investigate the photocatalytic activity. The photocatalytic activity was done through dispersing of 45 mg photocatalyst powder in an 80 mL solution of dye (2.5 mg/L) in a glass reactor. It should be noticed that the solution was stirred in darkness for about 30 min to establish adsorption–desorption equilibrium between dye molecules and the surface of photocatalysts. Then, the solution was under irradiation for about 180 min while stirring constantly during irradiation to make a uniform mixture. The photocatalytic tests were applied at room temperature, and the setup was held in a chamber under a 15 W visible LED. During the photocatalytic experiment, each 15 min 3 mL of the solution was taken out to measure optical transmission spectra to reveal the concentration of dye by determining the maximum absorption wavelength of dyes. To evaluate the reusability of synthesized sample, cyclic photodegradation experiments of MeO on Bi_2O_3/ $Bi_2O_2CO_3$/$(BiO)_4CO_3(OH)_2$ nanocomposite were done under the same conditions. For doing cyclic photocatalysis tests, Bi_2O_3/$Bi_2O_2CO_3$/$(BiO)_4CO_3(OH)_2$ photocatalyst was withdrawn from the solution by means of the centrifuge after each cycle. The solution sample is centrifuged at 4500 RPM for 10 min, then washed and cleaned via ultra-sonicating of the sample in deionized water several times and, after drying, reused again in a new solution of MeO with photocatalyst. The photodegradation procedure of MeO by the sample was redone in four cycles. Furthermore, various scavengers were used to investigate the role of reactive oxidative species in the MeO degradation process by Bi_2O_3/$Bi_2O_2CO_3$/$(BiO)_4CO_3(OH)_2$. To capture the generated holes, hydroxyl and superoxide radicals, the ethylenediaminetetraacetic acid (EDTA), isopropyl alcohol (IPA) and benzoquinone (BQ) were used in the photocatalytic process, respectively.

Results and discussion

The type of functional groups on the surface of nanostructures was identified by FTIR spectra, as illustrated in Fig. 1. The FTIR spectra of synthesized samples in urea solution and water are compared. The Bi_2O_3/$Bi_2O_2CO_3$/ $(BiO)_4CO_3(OH)_2$ spectrum reveals characteristic vibrating modes of the free carbonate ion with point group symmetry D_{3h}. This is engrossed in several internal vibrations, including symmetric stretching mode ν_1 at 1066 cm^{-1}, out-of-plane bending mode ν_2 at 848 cm^{-1}, antisymmetric vibration ν_3 at 1460 and 1384 cm^{-1}, in-plane deformation ν_4 at 695 and 673 cm^{-1} and symmetric stretching plus in-plane deformation modes, $\nu_1 + \nu_4$, at 1756 and 1730 cm^{-1}[41, 42, 47]. The band groups of CO_3^{-2} at ν_1, ν_2, ν_3, ν_4 and $\nu_1 + \nu_4$ reveal the formation of $Bi_2O_2CO_3$. Moreover, the bands at 844 cm^{-1} and 300–800 cm^{-1} correspond to Bi-O-C and stretching modes of the Bi-O bonds in $Bi_2O_2CO_3$, and Bi_2O_3, respectively [60]. The broad bands at 3600–3300 cm^{-1} and 1400 cm^{-1} are corresponding to O–H stretching vibration and O–H bending vibration, respectively, suggesting the presence of $(BiO)_4CO_3(OH)_2$ in composition [61, 62].

The XRD patterns of synthesized samples are illustrated in Fig. 2. It is observed that there are different phases in the pattern of synthesized sample in water, which are related to the crystallographic characteristics of the Bi, Bi_2O_3 and $Bi(OH)_3$ phases. The diffraction peaks assigned to Bi, α-Bi_2O_3, β-Bi_2O_3 and $Bi(OH)_3$ are based on JCPDS NO. 00-005-0519, 01-071-2274, 00-027-0050 and 00-001-0898 standard cards. The crystallographic parameters of the bismuth phase are rhombohedral, $a = b = 4.5460$ Å, $c = 11.86$ Å, $\alpha = \beta = 90°$ and $\gamma = 120°$. Bismuth oxide formed in two crystal systems, monoclinic with $a = 5.8486$, $b = 8.1661$ and $c = 7.5097$ Å, $\alpha = \gamma = 90°$, $\beta = 113°$ and tetragonal with $a = b = 7.7420$, $c = 5.6310$ Å, $\alpha = \gamma = 90°$ and $\beta = 113$. In comparison with the pattern of synthesized sample in water, the pattern of the synthesized sample in urea solution reveals α-Bi_2O_3, $(BiO)_4CO_3(OH)_2$ and $Bi_2O_2CO_3$ phases. The α-Bi_2O_3 has the same reference code as that of synthesized in water [63]. The $(BiO)_4CO_3(OH)_2$ phase is relevant to 00-038-0579 reference code with orthorhombic crystal system and $a = 10.7716$, $b = 5.4898$, $c = 14.75740$ Å and $\alpha = \beta = \gamma = 90°$ crystallographic parameters [64]. The crystal structure of $Bi_2O_2CO_3$ is orthorhombic with a = 5.4680, b = 27.3200, c = 5.4680 Å, $\alpha = \beta = \gamma = 90°$ crystal parameters and is based on 01-084-1752 standard card [65]. Based on the calculation of semiquantitative analysis
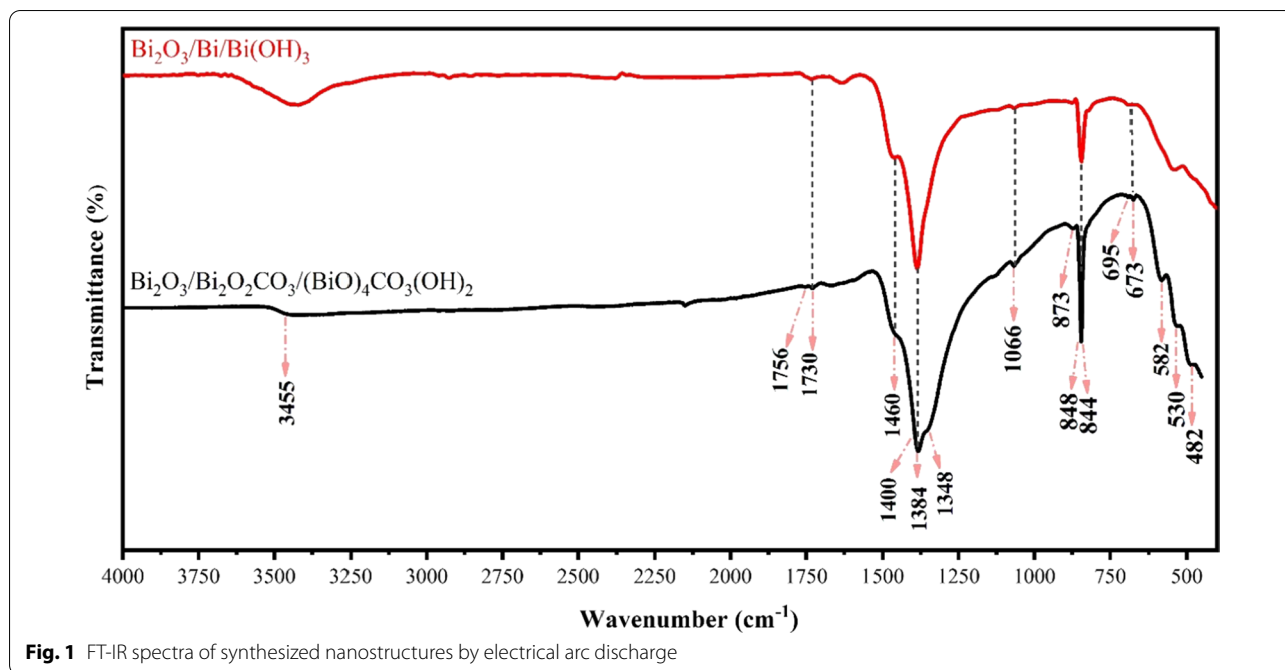
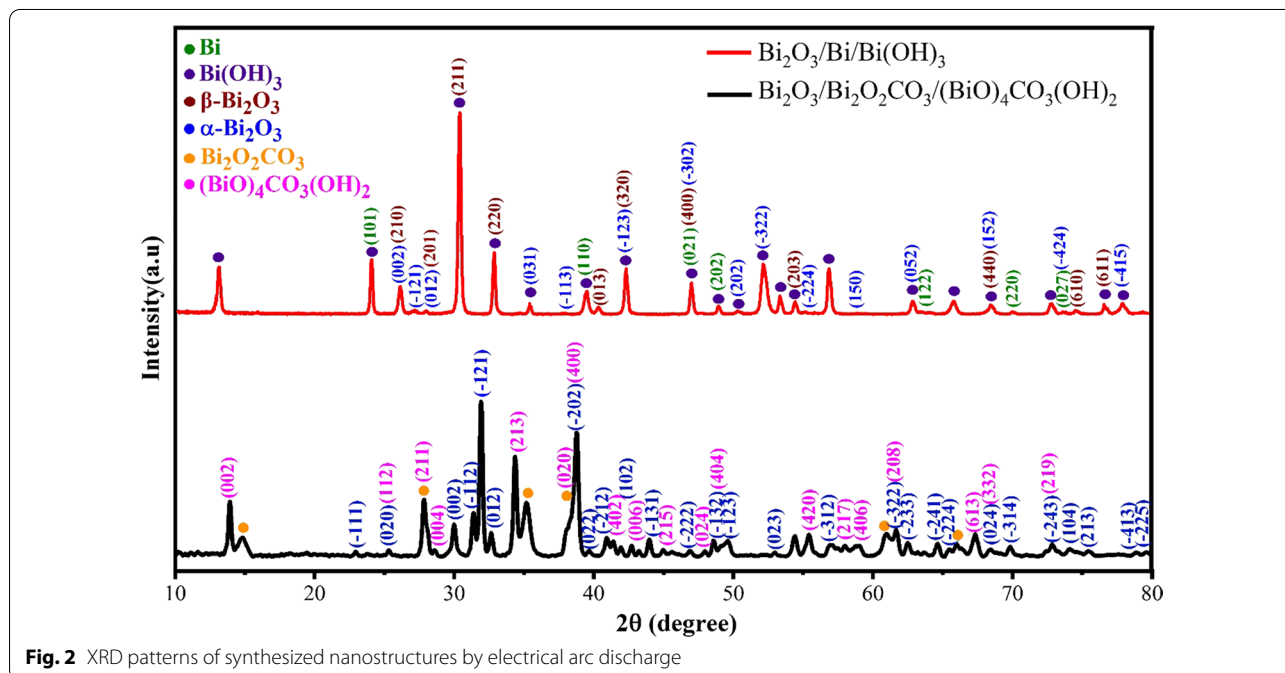**Fig. 1** FT-IR spectra of synthesized nanostructures by electrical arc discharge

Fig. 2 XRD patterns of synthesized nanostructures by electrical arc discharge

of multiphase systems, the α-Bi_2O_3, $(BiO)_4CO_3(OH)_2$ and $Bi_2O_2CO_3$ phases have 44%, 36% and 20% shares of structure, respectively. To describe the mechanism of multiphase formation of nanostructures, it should be noticed that establishing electrical arc discharge leads to the formation of a high-temperature plasma [59]. The plasma dissipates the solution molecules and produces neutral, ionic and molecular species of bismuth, water and urea. Formation of Bi, O, C and H ions or OH, H_2, O_2, CO and CO_2 molecules in their ground or excited state in the plasma of electric arc discharge has been reported before [53, 57]. So, based on these species, the formation

Hashemi *et al. Nanoscale Research Letters*   (2022) 17:75

Page 6 of 16

of oxide, oxide carbonate, hydroxide and carbonate oxide of bismuth could be explained.

Figure 3 shows the FE-SEM images of samples with different magnifications and size distribution histogram of the synthesized sample in urea solution. The FE-SEM images were obtained after keeping samples in their solutions for 15 days. The $Bi_2O_3/Bi_2O_2CO_3/(BiO)_4CO_3(OH)_2$ has a nanoflake structure, and the approximate average thickness of nanoflakes was demonstrated by a size distribution histogram which was obtained by applying a Gaussian curve on the size histogram. The average thickness of $Bi_2O_3/Bi_2O_2CO_3/(BiO)_4CO_3(OH)_2$ nanoflakes is almost 22.0 ± 0.5 nm. The synthesized sample in water shows a nanoflake structure as well. Even though both samples indicate flake morphology, the $Bi_2O_3/Bi/Bi(OH)_3$ is considerably more agglomerated than $Bi_2O_3/Bi_2O_2CO_3/(BiO)_4CO_3(OH)_2$ nanocomposite. By increasing the agglomeration of nanostructures, the specific surface area will be reduced which will lead to less photocatalytic performance. Furthermore, FE-SEM elemental mapping and energy-dispersive spectrometry of synthesized nanoflakes in urea solution indicated the uniform distribution of Bi, O and C elements in the structure, as shown in Fig. 4.

Figure 5a and b shows the TEM image of $Bi_2O_3/Bi_2O_2CO_3/(BiO)_4CO_3(OH)_2$ nanoflakes with different magnifications, which confirms the SEM observation. With the formation of nanostructures with the more effective surface area, the interaction with dye molecules will increase. Therefore, it can be expected that by increasing the photocatalytic reaction sites, photocatalytic activity will improve [66, 67, 68]. Hence, the $Bi_2O_3/Bi_2O_2CO_3/(BiO)_4CO_3(OH)_2$ with fine flake morphology will have more photocatalytic reaction sites and thus better photocatalytic performance than $Bi_2O_3/Bi/Bi(OH)_3$.

Optical properties, especially the UV–visible spectrum of the samples, are an effective way to evaluate photocatalytic activity via measuring light harvesting efficiency over different ranges of visible spectrum [53]. The optical absorption spectra of colloidal samples over different times immediately after synthesis, 15 min, 30 min, 1 h, 4 h and 4 days are shown in Fig. 6. The spectra are shown at a wavelength between 190 and 900 nm. The intensity and wavelength of the optical absorption peak as well as the form of the spectrum depend on the morphology, size, material type of nanostructures and dielectric function of the surrounding medium [69]. The optical absorption spectra of the samples show an intense absorption at wavelengths between 190 and 400 nm, which is explained by electron transitions from the valance band to the conduction band of $Bi_2O_3/Bi_2O_2CO_3/(BiO)_4CO_3(OH)_2$ and $Bi_2O_3/Bi/Bi(OH)_3$, which is the feature of semiconductor materials [26, 43, 60]. The intense absorption edge

of both samples reveals their proper visible light absorbing ability. In addition, noble metallic nanoparticles reveal an absorption peak in the UV–visible spectrum which is explained by surface plasmon resonance (SPR) [70]. According to XRD results of synthesized sample in water the formation of bismuth phase in fresh samples are probable, hence the observable peak around 200 nm can be attributed to SPR of metallic bismuth phase in both samples [54]. The occurred changes in the absorption spectra can be explained by the disappearing of the bismuth plasmon absorption peak by oxidation of nanostructures. The optical properties and absorption edge of $Bi_2O_3/Bi_2O_2CO_3/(BiO)_4CO_3(OH)_2$ show that synthesized nanoflakes in urea solution can be a good candidate for visible light harvesting and possible photocatalytic activity than $Bi_2O_3/Bi/Bi(OH)_3$.

The photocatalytic activity of the novel $Bi_2O_3/Bi_2O_2CO_3/(BiO)_4CO_3(OH)_2$ nanoflakes with multi-heterojunctions and $Bi_2O_3/Bi/Bi(OH)_3$ nanocomposite was evaluated by the degradation of MeO under visible light irradiation for 180 min. In addition, to reveal the capacity of $Bi_2O_3/Bi_2O_2CO_3/(BiO)_4CO_3(OH)_2$ for use as a proper photocatalyst in environmental applications, the photocatalytic performance of $Bi_2O_3/Bi_2O_2CO_3/(BiO)_4CO_3(OH)_2$ investigated for the degradation of RB as well. The optical transmission spectra of MeO solution during the degradation process by $Bi_2O_3/Bi_2O_2CO_3/(BiO)_4CO_3(OH)_2$ nanoflakes exhibited considerable photocatalytic activity compared to that of $Bi_2O_3/Bi/Bi(OH)_3$. The MeO and RB absorption peaks at 464 and 530 nm were considerably reduced by $Bi_2O_3/Bi_2O_2CO_3/(BiO)_4CO_3(OH)_2$ photocatalyst. The concentration of the dye at different times during degradation can be obtained by Langmuir–Hinshelwood model [71]:

$$r = -\frac{dC(t)}{dt} = k_{abc}C(t) \tag{1}$$

where r is the degradation rate of the dye, $C(t)$ reveals the concentration of dye at time t and k_{abc} is a constant for reaction rate. The degradation kinetics of the dye can be described by the following equation at low concentration of the dye:

$$\ln\left(\frac{C_0}{C}\right) = k_{abs}t \tag{2}$$

where C_0 is the initial concentration of dye. The photocatalytic activity and dye degradation kinetics for the samples are presented in Fig. 7, which were obtained at different reaction times during the photodegradation process. Figure 7a illustrates the C/C_0 plot versus irradiation time and, as obviously seen, $Bi_2O_3/Bi_2O_2CO_3/(BiO)_4CO_3(OH)_2$ shows a highly efficient degradation rate. Figure 7b shows the degradation reaction kinetics,
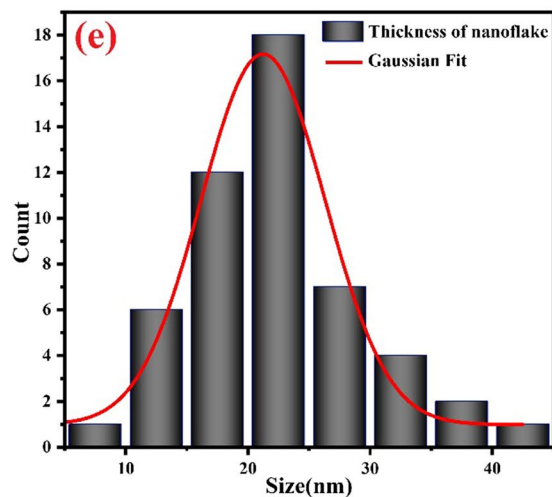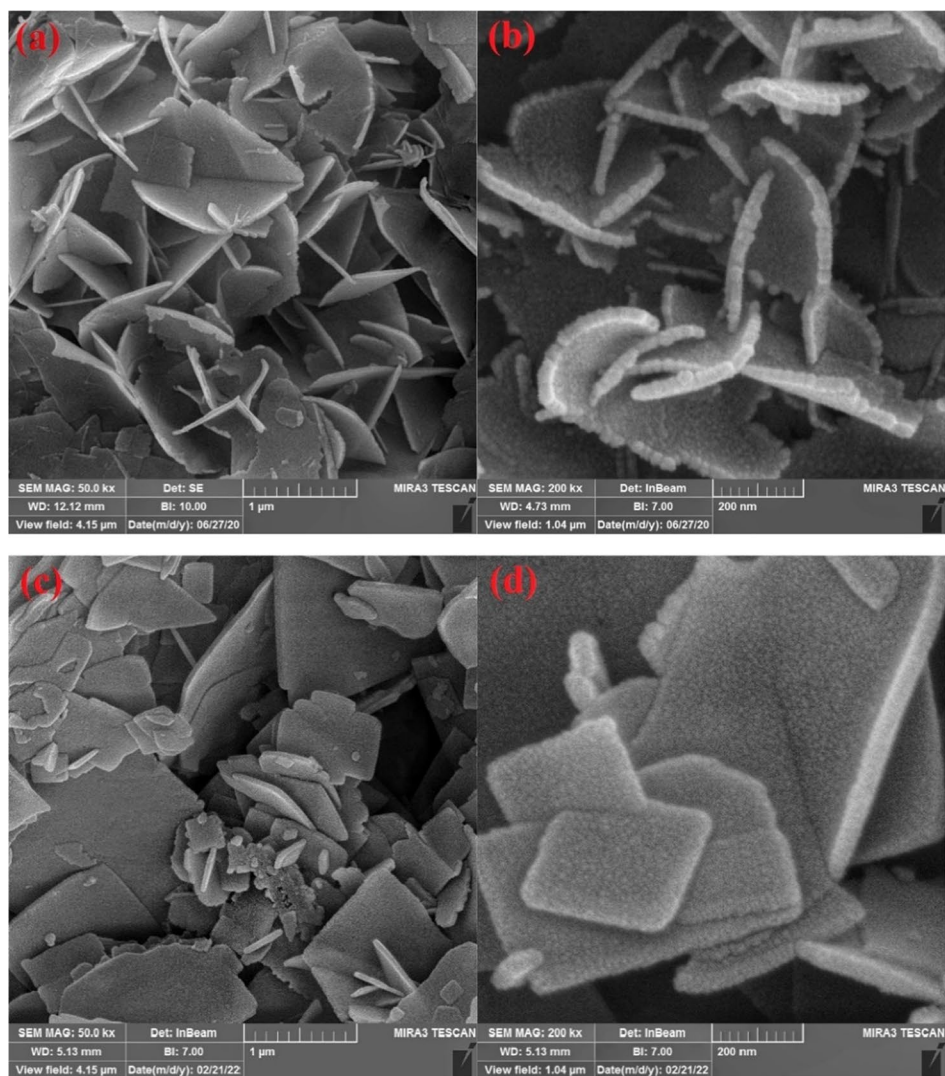
Fig. 3 FE-SEM images of synthesized nanostructures by electrical arc discharge in **a**, **b** urea solution, **c**, **d** water, and **e** size distribution histogram of $Bi_2O_3/Bi_2O_2CO_3/(BiO)_4CO_3(OH)_2$ nanoflakes
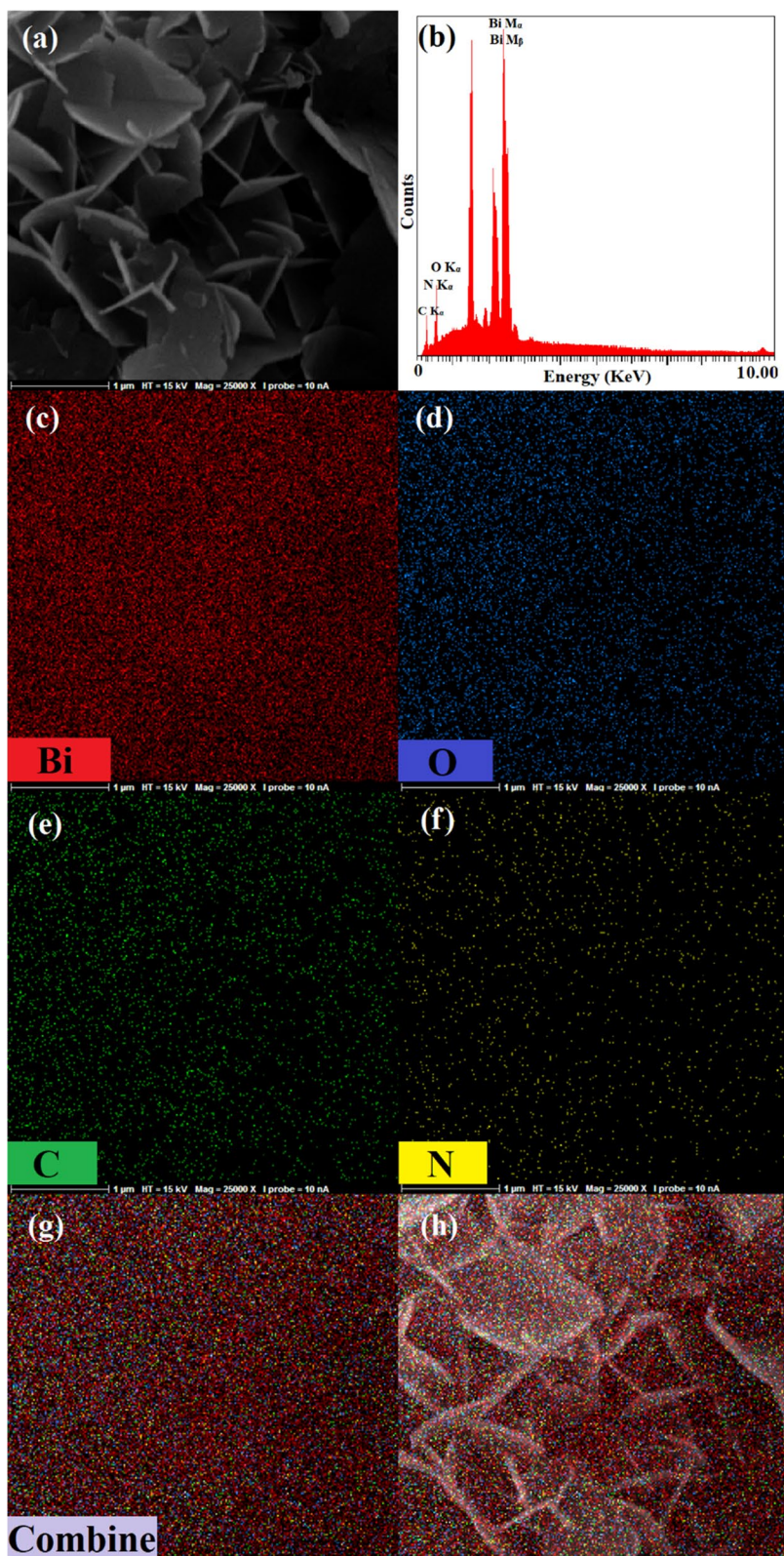
Fig. 4 **a** FE-SEM image, **b** EDS spectrum, elemental mapping patterns of **c** Bi, **d** O, **e** C, **f** N, **g** combine and **h** combine with FE-SEM image of Bi_2O_3/$Bi_2O_2CO_3$/$(BiO)_4CO_3(OH)_2$ nanoflakes

Hashemi *et al. Nanoscale Research Letters*   (2022) 17:75

Page 9 of 16
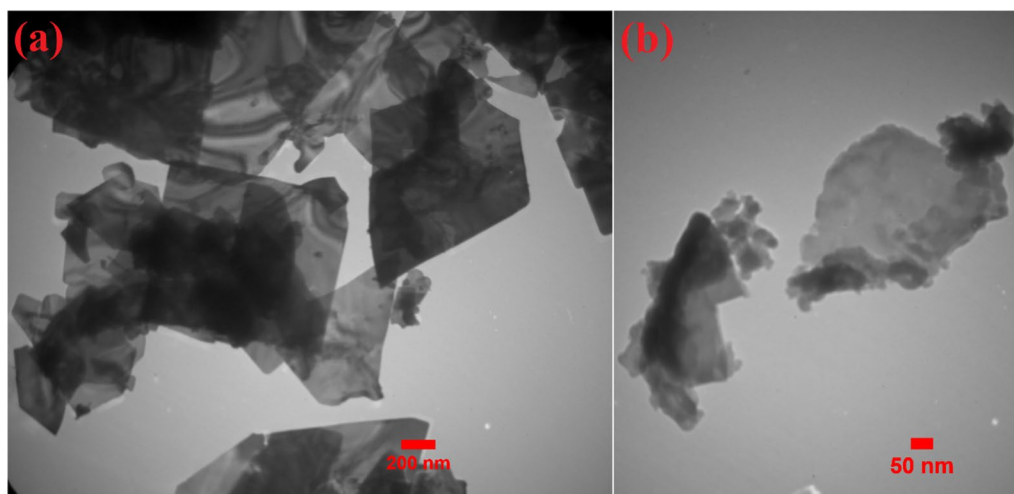
Fig. 5 TEM images of $Bi_2O_3/Bi_2O_2CO_3/(BiO)_4CO_3(OH)_2$ nanoflakes with different magnifications, **a** 200 nm and **b** 50 nm
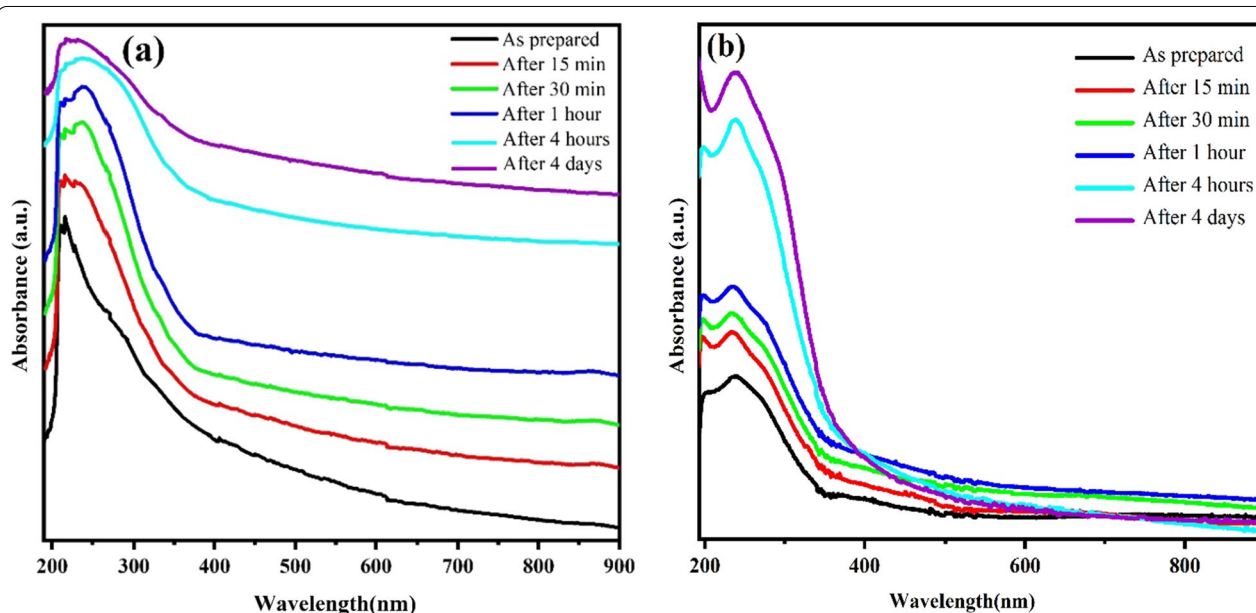

Fig. 6 UV–visible optical absorption spectra of synthesized colloidal samples in **a** urea solution, **b** water, over different times

which were measured from the slopes of the $-\ln(C/C_0)$ plots versus irradiation time [72]. The calculated k_{abs} values for photodegradation of MeO and RB on $Bi_2O_3/Bi_2O_2CO_3/(BiO)_4CO_3(OH)_2$ are 5.2×10^{-3} min^{-1} and 4.9×10^{-3} min^{-1}, respectively, and for photodegradation of MeO on $Bi_2O_3/Bi/Bi(OH)_3$ is 2.0×10^{-3} min^{-1}. The promoted photocatalytic performance of $Bi_2O_3/Bi_2O_2CO_3/(BiO)_4CO_3(OH)_2$ can be attributed to its composition, absorption edge, flake morphology and multiphase structure. Based on the obtained results of

this research, it can be concluded that the formation of multi-heterojunction can efficiently improve the photocatalytic activity of $Bi_2O_3/Bi_2O_2CO_3/(BiO)_4CO_3(OH)_2$ photocatalyst in comparison with $Bi_2O_3/Bi/Bi(OH)_3$ photocatalyst. In addition, these results can be compared with other photocatalysts such as nanosheet $Bi_2O_2CO_3$ and microrod $BiOHC_2O_4/Bi_2O_2CO_3$ with photocatalytic performance for the removal of MeO in 50 mL aqueous solution of 10 ppm dye under 400 W xenon lamp irradiation. Hierarchical $BiOHC_2O_4/Bi_2O_2CO_3$

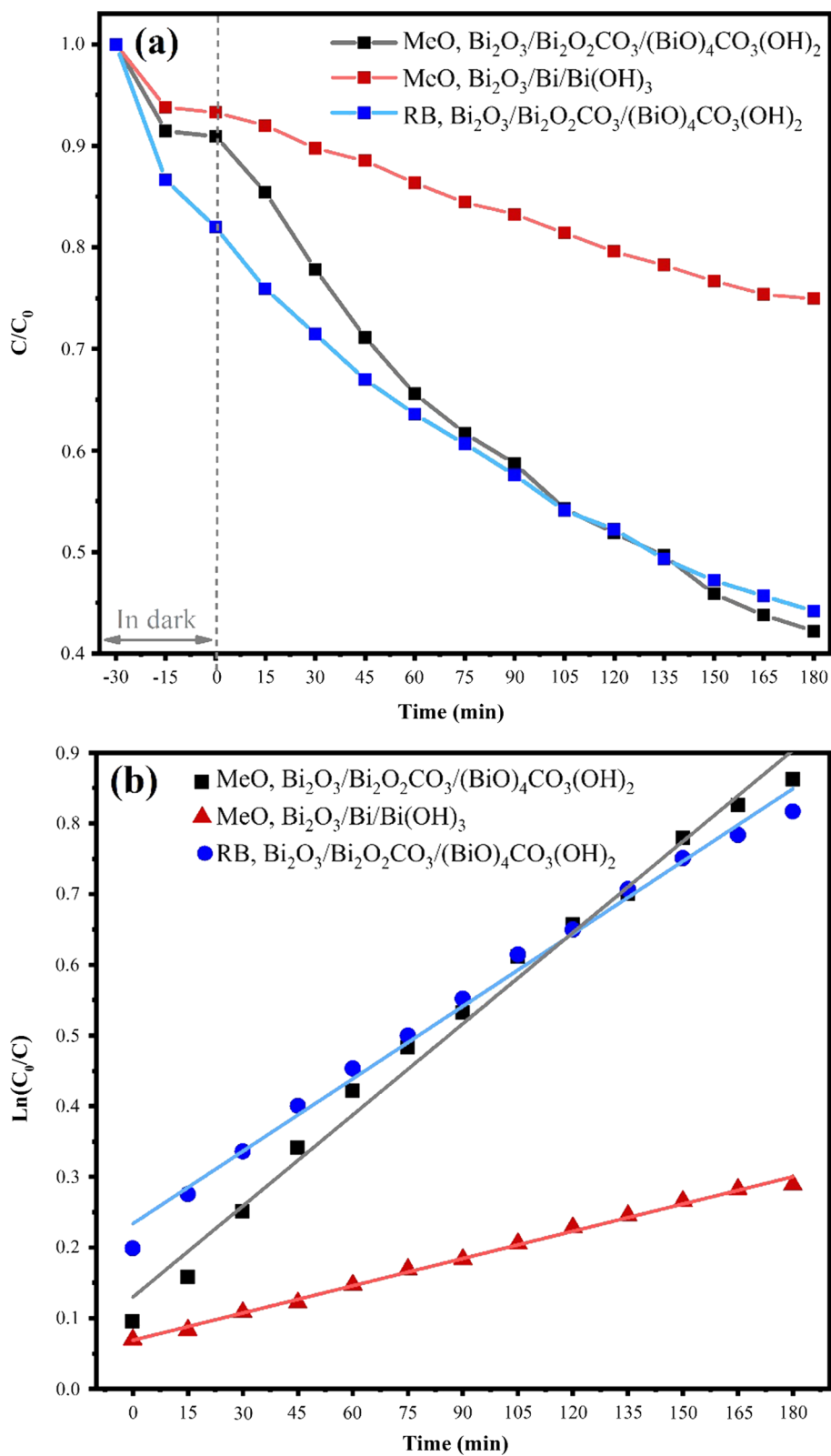Hashemi *et al. Nanoscale Research Letters* (2022) 17:75

Page 10 of 16

Fig. 7 **a** Photocatalytic degradation of dyes and **b** Liner curves of ln(C/C_0) versus the irradiation time for the photodegradation reaction kinetics of dyes by samples
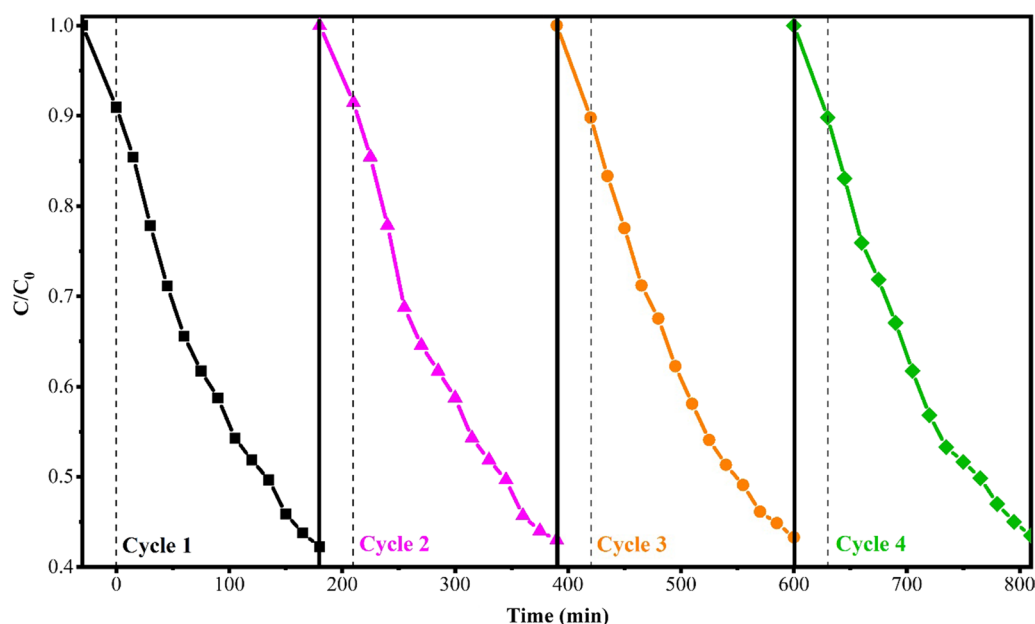
Fig. 8 Photocatalytic stability test of $Bi_2O_3/Bi_2O_2CO_3/(BiO)_4CO_3(OH)_2$ photocatalyst

heterostructure revealed the highest degradation kinetic with 4.7×10^{-3} min^{-1} values, which was considerably higher than single $BiOHC_2O_4$ and $Bi_2O_2CO_3$ [73]. For silver-doped Bi_2O_3 photocatalysts with nanosheet morphology in photodegradation of MeO with 20 mg L^{-1} concentration under a 500 W Xenon arc lamp over 180-min irradiation time, the obtained degradation rate was less than 4×10^{-3} min^{-1} in the most optimal state [74]. Degussa P25 titania was used for the removal of rhodamine B with 10 mg in 50 mL water solution under irradiation of 500 W Mercury-Xenon lamp with 6.4×10^{-4} min^{-1} degradation rate [8]. In all of these examples, the power of light sources was around 500 W while the photocatalytic results of this research obtained under only 15 W visible LED.

The recyclability and reusability of photocatalysts are important factors in practical applications [75, 76]. The stability of the photocatalytic activity of a photocatalyst can be evaluated through the monitoring of photocatalytic degradation of MeO under light over several cycles. In fact, the stability of a photocatalyst can be proved over every cyclic photocatalytic degradation test [77]. Hence, efficiency should not decline noticeably with each cycle. The degradation efficiency of the recovered $Bi_2O_3/Bi_2O_2CO_3/(BiO)_4CO_3(OH)_2$ photocatalyst after four cycles is shown in Fig. 8. As it is clear, after each cycle the photocatalytic activity of the sample was almost unchanged, which demonstrates high stability of photocatalyst after multiple reuse.

The possible photocatalytic degradation mechanism of MeO by $Bi_2O_3/Bi_2O_2CO_3/(BiO)_4CO_3(OH)_2$ under visible light irradiation was investigated through trapping experiments of reactive species in photocatalytic tests by using of different radical scavengers, namely EDTA, IPA and BQ for scavenging the active h^+, $^{\bullet}OH$ and $^{\bullet}O_2^{-}$ during the photocatalytic reaction [26, 43]. Based on Fig. 9, degradation values of the MeO decreased in all capturing experiments, which reveals that all the generated reactive species are effective in photodegradation of MeO. However, BQ as a superoxide radical scavenger plays more important role in the MeO degradation. As shown in Fig. 9, by capturing $^{\bullet}O_2^{-}$ the dye degradation will dwindle more than other h^+, $^{\bullet}OH$ species.

The photocatalytic performance is deeply depend on the electronic and energy band structure of the semiconductor. Mott–Schottky measurements can be used to better study the energy band structure of a semiconductor. For instance, the band structure of S-scheme BP/BiOBr nano-heterojunction with photocatalytic performance in the degradation of tetracycline and evolution of oxygen, the flat-band potential of BPQDs and CN in CN/rGO@BPQDs high–low junctions system with photocatalytic degradation and H_2O_2 production, as well as study of semiconductor type and flat-band potential of S-C_3N_4 and PDI-Ala of S-Scheme heterojunction PDI-Ala/S-C_3N_4 organic photocatalyst in photodegradation of tetracycline and p-nitrophenol and production of H_2O_2 under visible-light irradiation, were measured by the Mott–Schottky method [78, 79, 80]. Although this method has a
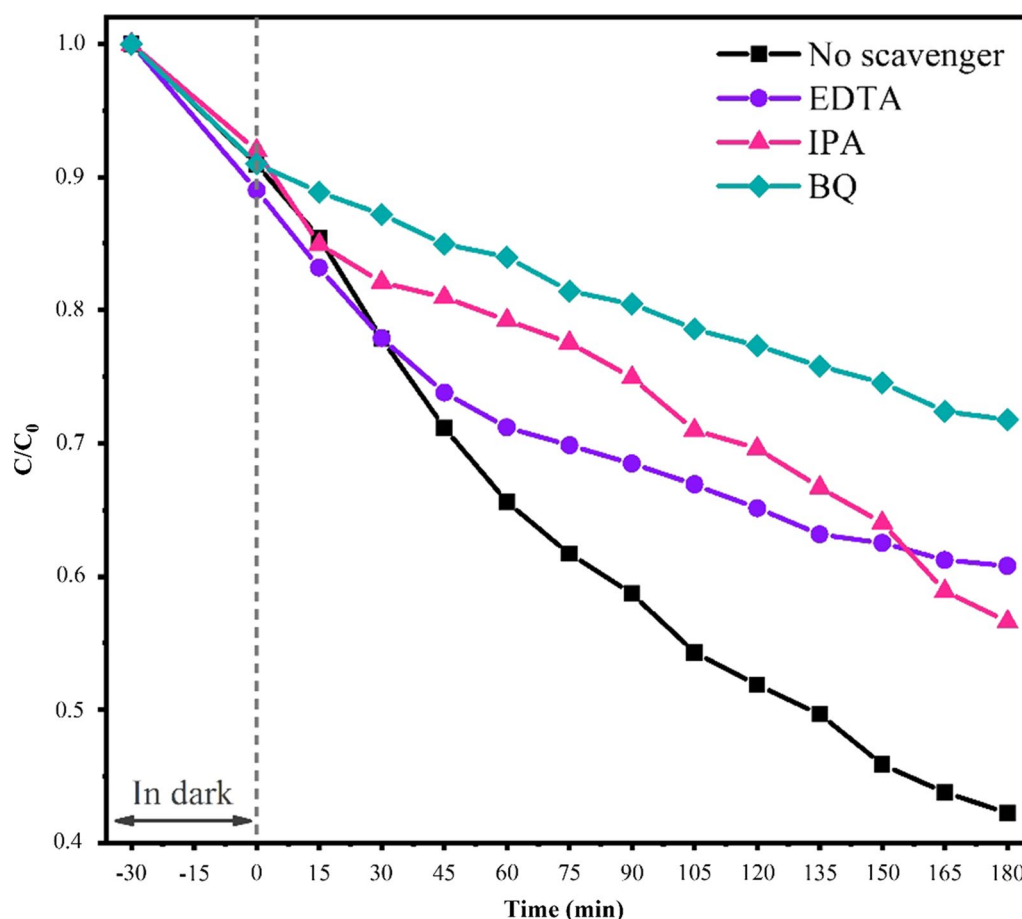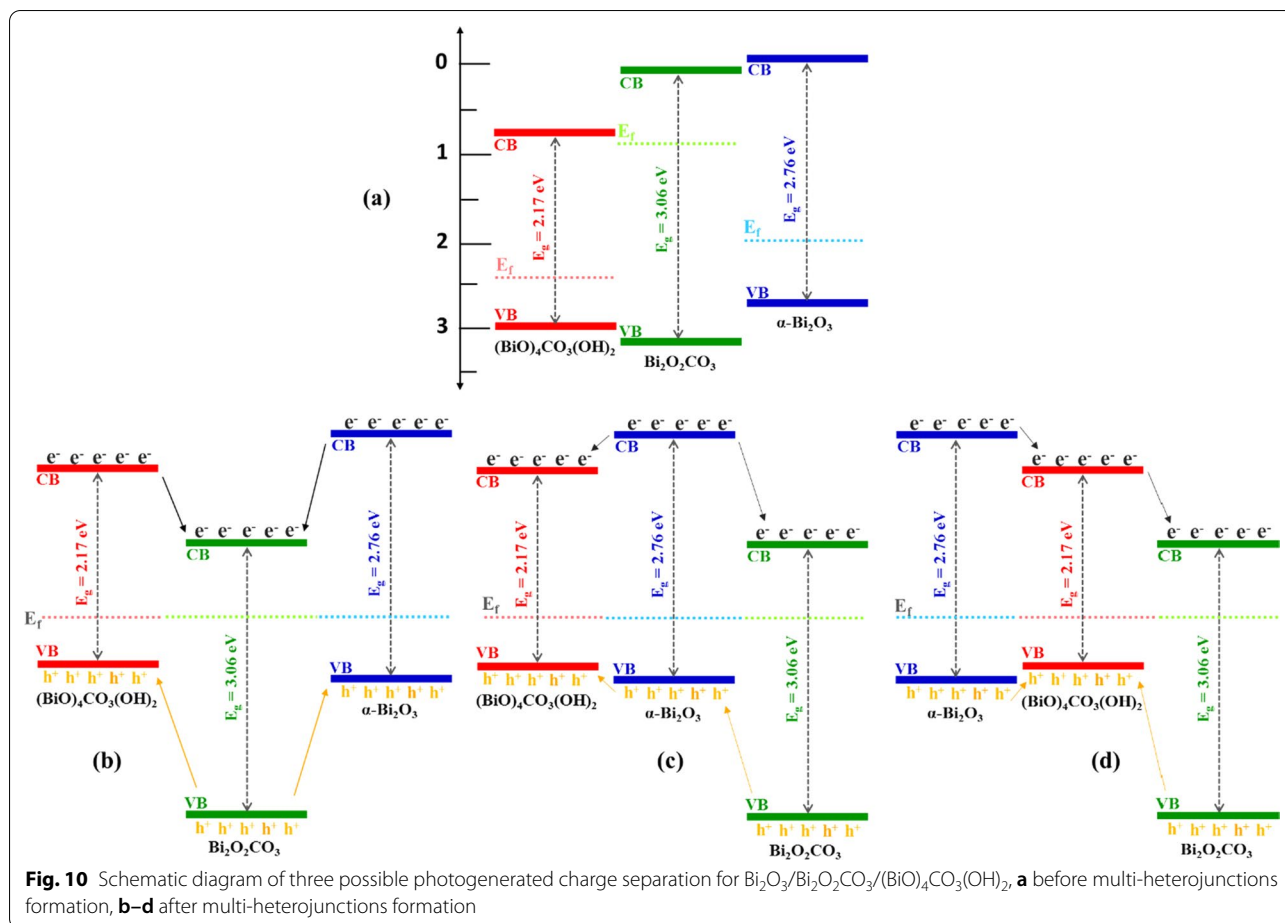
Hashemi *et al. Nanoscale Research Letters*   (2022) 17:75

Page 12 of 16

Fig. 9 Degradation curves of MeO with different scavengers under the visible light by $Bi_2O_3/Bi_2O_2CO_3/(BiO)_4CO_3(OH)_2$ photocatalyst

lot of advantages, it has been used for revealing the band structure of a single component in a multi-component system, while in the present work, the multi-heterojunction $Bi_2O_3/Bi_2O_2CO_3/(BiO)_4CO_3(OH)_2$ nanocomposite has been synthesized during the in situ arc discharge process and there is no chance for the synthesis of single phases with this method. Therefore, the probable band structure of $Bi_2O_3/Bi_2O_2CO_3/(BiO)_4CO_3(OH)_2$ according to the calculated band gap energy level of it and the energy levels of literature are proposed in three possible degradation mechanisms. The energy band structure of $Bi_2O_3/Bi_2O_2CO_3/(BiO)_4CO_3(OH)_2$ multi-heterojunction before and after junction are proposed in Fig. 10 [26, 81, 82]. The Fermi level of α-Bi_2O_3 and $(BiO)_4CO_3(OH)_2$ which are p-type photocatalysts are close to the valence band, and the Fermi level of n-type $Bi_2O_2CO_3$ is close to the conduction band [26, 83]. By formation of multi-heterojunction, the energy band of α-Bi_2O_3, $(BiO)_4CO_3(OH)_2$ and $Bi_2O_2CO_3$ will move upward or downward to reach an equilibration state of Fermi level [26]. Under visible light irradiation, the photogenerated

electrons in the conduction band of phases will transfer to downer CB, while the holes in the valence band are likely to transfer to the opposite position [82]. In this situation, the recombination of photogenerated carriers in photocatalyst will reduce and thus the formation of p-n-p or p-p-n $Bi_2O_3/Bi_2O_2CO_3/(BiO)_4CO_3(OH)_2$ multi-heterojunction nanoflakes will improve the separation efficiency of the photogenerated electrons and holes which lead better photocatalytic performance.

The PL spectrum of the $Bi_2O_3/Bi_2O_2CO_3/(BiO)_4CO_3(OH)_2$ with the excitation wavelength at 355 nm was measured and compared with the PL spectrum of $Bi_2O_3/Bi/Bi(OH)_3$ to display the photoactivity enhancement mechanism. Broad emission peaks in the range between 2 and 3 eV are found in the PL spectra of the samples, which is in agreement with the documents [24, 43, 51, 84]. In general, a superior PL intensity shows an upper recombination rate of photogenerated electrons and holes, and thus lower PL intensity expresses a lower recombination rate of photogenerated electrons and holes, which means an improved separation rate of electrons and holes and so better photocatalytic performance [43].

Fig. 10 Schematic diagram of three possible photogenerated charge separation for $Bi_2O_3/Bi_2O_2CO_3/(BiO)_4CO_3(OH)_2$, **a** before multi-heterojunctions formation, **b–d** after multi-heterojunctions formation

Based on PL spectra shown in Fig. 11, the PL intensities of the multi-heterojunction $Bi_2O_3/Bi_2O_2CO_3/(BiO)_4CO_3(OH)_2$ nanoflakes are all lower than that of the $Bi_2O_3/Bi/Bi(OH)_3$ at the same condition, which means the efficient separation rate of the carriers in $Bi_2O_3/Bi_2O_2CO_3/(BiO)_4CO_3(OH)_2$. The formation of the multi-heterojunction reduces the recombination rate of photogenerated electrons and holes and then is favorable to improving photocatalytic activity.

Conclusion

In summary, new multi-heterojunction $Bi_2O_3/Bi_2O_2CO_3/(BiO)_4CO_3(OH)_2$ nanoflakes were prepared by applying a 40 A DC current between two bismuth electrodes through DC electrical arc discharge in urea solution and investigated for using them as a visible light photocatalyst. The photocatalytic performance of $Bi_2O_3/Bi_2O_2CO_3/(BiO)_4CO_3(OH)_2$ is compared with that of $Bi_2O_3/Bi/Bi(OH)_3$ which is synthesized in the same condition in water. FT-IR, XRD and EDS results revealed the formation of α-Bi_2O_3, $Bi_2O_2CO_3$ and $(BiO)_4CO_3(OH)_2$ phases. FE-SEM and TEM analysis revealed the fine flake morphology of $Bi_2O_3/Bi_2O_2CO_3/(BiO)_4CO_3(OH)_2$ with a

Fig. 11 Photoluminescence spectra of synthesized nanostructures by electrical arc discharge in urea solution and water

Hashemi *et al. Nanoscale Research Letters*   (2022) 17:75

Page 14 of 16
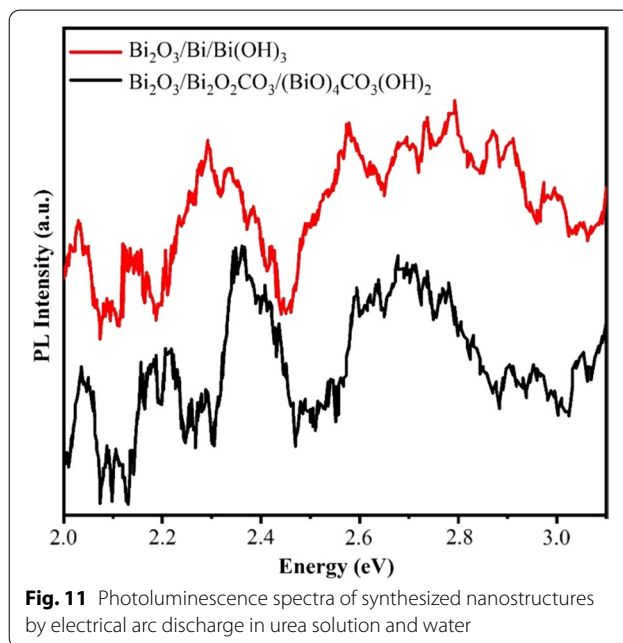
thickness of about 22.0 ± 0.5 nm. The optical absorption spectra of the samples show an absorption edge at a wavelength between 190 and 400 nm. The XRD and PL results confirm the formation of multi-heterojunction between α-Bi_2O_3, $Bi_2O_2CO_3$ and $(BiO)_4CO_3(OH)_2$ phases. In comparison with $Bi_2O_3/Bi/Bi(OH)_3$, the $Bi_2O_3/Bi_2O_2CO_3/(BiO)_4CO_3(OH)_2$ nanoflakes reveal lower agglomerated morphology, better absorption edge and lower recombination rate and thus much better photocatalytic activity. The results of this research introduce a novel multi-heterojunction compound with considerable multi-applicable photocatalytic performance in environmental applications via an appropriate and cost-effective synthesis method.

Abbreviations

DC: Direct current; IEF: Internal electric field; MeO: Methylene orange; FT-IR: Fourier-transform infrared spectroscopy; XRD: X-ray diffraction; FE-SEM: Field emission scanning electron microscopy; EDS: Energy dispersive spectroscopy; TEM: Transmission electron microscopy; PL: Photoluminescence; EDTA: Ethylenediaminetetraacetic acid; IPA: Isopropyl alcohol; BQ: Benzoquinone (BQ).

Author contributions

EH carried out the synthesis processes, analysis and photocatalytic processes of dye decomposition. RP and HD supervised synthesis, analyses of the materials and preparation of the manuscript. All authors discussed the results and contributed a revision of the manuscript. All authors read and approved the final manuscript.

Availability of Data and Materials

The datasets used and/or analyzed during the current study are available from the corresponding author on reasonable request.

Declarations

Ethics Approval and Consent to Participate
Not applicable.

Consent for Publication
Not applicable.

Competing interests
The authors declare no competing interests.

References

1. Qin Z, Su T, Ji H (2018) Photocatalytic nanomaterials for the energy and environmental application. In: Guo Z, Chen Y, Lu NL (eds) Multifunctional nanocomposites for energy and environmental applications. Wiley, Weinheim, pp 353–401
2. Pang H, Wei C, Li X et al (2015) Microwave-assisted synthesis of NiS_2 nanostructures for supercapacitors and cocatalytic enhancing photocatalytic H_2 production. Sci Rep 4:3577. https://doi.org/10.1038/srep03577
3. Rashid J, Parveen N, Iqbal A et al (2019) Facile synthesis of g-C_3N_4(0.94)/CeO_2(0.05)/Fe_3O_4(0.01) nanosheets for DFT supported visible photocatalysis of 2-Chlorophenol. Sci Rep 9:10202. https://doi.org/10.1038/s41598-019-46544-7
4. Chen M, Liu P, He J-H et al (2021) Nanofiber template-induced preparation of ZnO nanocrystal and its application in photocatalysis. Sci Rep 11:21196. https://doi.org/10.1038/s41598-021-00303-9
5. Li X, Kang B, Dong F et al (2021) Enhanced photocatalytic degradation and H_2/H_2O_2 production performance of S-pCN/$WO_{2.72}$ S-scheme heterojunction with appropriate surface oxygen vacancies. Nano Energy 81:105671. https://doi.org/10.1016/j.nanoen.2020.105671
6. Acharya R, Parida K (2020) A review on TiO_2/g-C_3N_4 visible-light- responsive photocatalysts for sustainable energy generation and environmental remediation. J Environ Chem Eng 8:103896. https://doi.org/10.1016/j.jece.2020.103896
7. Raizada P, Sharma S, Kumar A et al (2020) Performance improvement strategies of $CuWO_4$ photocatalyst for hydrogen generation and pollutant degradation. J Environ Chem Eng 8:104230. https://doi.org/10.1016/j.jece.2020.104230
8. Basith MA, Ahsan R, Zarin I, Jalil MA (2018) Enhanced photocatalytic dye degradation and hydrogen production ability of $Bi_{25}FeO_{40}$-rGO nanocomposite and mechanism insight. Sci Rep 8:11090. https://doi.org/10.1038/s41598-018-29402-w
9. Carneiro JO, Teixeira V, Carvalho P et al (2011) Self-cleaning smart nanocoatings. In: Makhlouf ASH, Tiginyanu I (eds) Nanocoatings and ultra-thin films. Elsevier, pp 397–413
10. Guo Y, Yan B, Deng F et al (2022) Lattice expansion boosting photocatalytic degradation performance of $CuCo_2S_4$ with an inherent dipole moment. Chin Chem Lett. https://doi.org/10.1016/j.cclet.2022.04.066
11. Borges ME, Sierra M, Cuevas E et al (2016) Photocatalysis with solar energy: Sunlight-responsive photocatalyst based on TiO_2 loaded on a natural material for wastewater treatment. Sol Energy 135:527–535. https://doi.org/10.1016/j.solener.2016.06.022
12. Gutierrez-Mata AG, Velazquez-Martínez S, Álvarez-Gallegos A et al (2017) Recent overview of solar photocatalysis and solar photo-fenton processes for wastewater treatment. Int J Photoenergy 2017:1–27. https://doi.org/10.1155/2017/8528063
13. Mills A, Le Hunte S (1997) An overview of semiconductor photocatalysis. J Photochem Photobiol A 108:1–35. https://doi.org/10.1016/S1010-6030(97)00118-4
14. Hoffmann MR, Martin ST, Wonyong C, Bahnemann DW (1995) Environmental applications of semiconductor photocatalysis. Chem Rev 95:69–96. https://doi.org/10.1021/cr00033a004
15. Meng X, Zhang Z (2016) Bismuth-based photocatalytic semiconductors: introduction, challenges and possible approaches. J Mol Catal A Chem 423:533–549. https://doi.org/10.1016/j.molcata.2016.07.030
16. Mehring M (2007) From molecules to bismuth oxide-based materials: potential homo- and heterometallic precursors and model compounds. Coord Chem Rev 251:974–1006. https://doi.org/10.1016/j.ccr.2006.06.005
17. Reverberi AP, Varbanov PS, Vocciante M, Fabiano B (2018) Bismuth oxide-related photocatalysts in green nanotechnology: a critical analysis. Front Chem Sci Eng 12:878–892. https://doi.org/10.1007/s11705-018-1744-5
18. Jansi Rani B, Babu ES, Praveenkumar M et al (2020) Morphology-dependent photoelectrochemical and photocatalytic performance of γ-Bi_2O_3 nanostructures. J Nanosci Nanotechnol 20:143–154. https://doi.org/10.1166/jnn.2020.17188
19. Khairnar SD, Shrivastava VS (2019) Photocatalytic degradation of chlorpyrifos and methylene blue using α-Bi_2O_3 nanoparticles fabricated by sol–gel method. SN Appl Sci 1:762. https://doi.org/10.1007/s42452-019-0761-4
20. Schlesinger M, Schulze S, Hietschold M, Mehring M (2013) Metastable β-Bi_2O_3 nanoparticles with high photocatalytic activity from polynuclear bismuth oxido clusters. Dalton Trans 42:1047–1056. https://doi.org/10.1039/C2DT32119J
21. Oudghiri-Hassani H, Rakass S, Al Wadaani FT et al (2015) Synthesis, characterization and photocatalytic activity of α-Bi_2O_3 nanoparticles. J Taibah Univ Sci 9:508–512. https://doi.org/10.1016/j.jtusci.2015.01.009
22. Jalalah M, Faisal M, Bouzid H et al (2015) Comparative study on photocatalytic performances of crystalline α- and β-Bi_2O_3 nanoparticles under visible light. J Ind Eng Chem 30:183–189. https://doi.org/10.1016/j.jiec.2015.05.020
23. Margha FH, Radwan EK, Badawy MI, Gad-Allah TA (2020) Bi_2O_3—$BiFeO_3$ glass-ceramic: controllable β-/γ-Bi_2O_3 transformation and application

as magnetic solar-driven photocatalyst for water decontamination. ACS Omega 5:14625–14634. https://doi.org/10.1021/acsomega.0c01307

24. Liu G, Li S, Lu Y et al (2016) Controllable synthesis of α-Bi$_2$O$_3$ and γ-Bi$_2$O$_3$ with high photocatalytic activity by α-Bi$_2$O$_3$→γ-Bi$_2$O$_3$→α-Bi$_2$O$_3$ transformation in a facile precipitation method. J Alloys Compd 689:787–799. https://doi.org/10.1016/j.jallcom.2016.08.047

25. Eberl J, Kisch H (2008) Visible light photo-oxidations in the presence of α-Bi$_2$O$_3$. Photochem Photobiol Sci 7:1400. https://doi.org/10.1039/b811197a

26. Xu Z, Wang F, Zhang J et al (2020) In situ synthesis of p-n (BiO)$_4$CO$_3$(OH)$_2$/Bi$_2$O$_2$CO$_3$ internal polarized heterojunction for improved visible light photocatalytic performance. Mater Res Express 7:015910. https://doi.org/10.1088/2053-1591/ab62ec

27. Riente P, Fianchini M, Llanes P et al (2021) Shedding light on the nature of the catalytically active species in photocatalytic reactions using Bi$_2$O$_3$ semiconductor. Nat Commun 12:625. https://doi.org/10.1038/s41467-020-20882-x

28. Huang RZ, Wei YY, Gao TF et al (2021) Structure and electronic properties of δ-Bi$_2$O$_3$ tuned by vacancy and doping: a first-principles study. Ceram Int 47:205–213. https://doi.org/10.1016/j.ceramint.2020.08.123

29. Huang Y, Wang W, Zhang Q et al (2016) In situ fabrication of α-Bi$_2$O$_3$/(BiO)$_2$CO$_3$ nanoplate heterojunctions with tunable optical property and photocatalytic activity. Sci Rep 6:23435. https://doi.org/10.1038/srep23435

30. Yakout SM (2020) New efficient sunlight photocatalysts based on Gd, Nb, V and Mn doped alpha-Bi$_2$O$_3$ phase. J Environ Chem Eng 8:103644. https://doi.org/10.1016/j.jece.2019.103644

31. Munir S, Rasheed A, Zulfiqar S et al (2020) Synthesis, characterization and photocatalytic parameters investigation of a new CuFe$_2$O$_4$/Bi$_2$O$_3$ nanocomposite. Ceram Int. https://doi.org/10.1016/j.ceramint.2020.08.091

32. Lin Y-C, Peng C-K, Lim S-C et al (2021) Tailoring the surface oxygen engineering of a carbon-quantum-dot-sensitized ZnO@H-ZnO$_{1-x}$ multijunction toward efficient charge dynamics and photoactivity enhancement. Appl Catal B 285:119846. https://doi.org/10.1016/j.apcatb.2020.119846

33. Li X, Luo Q, Han L et al (2022) Enhanced photocatalytic degradation and H$_2$ evolution performance of N-CDs/S-C$_3$N$_4$ S-scheme heterojunction constructed by π–π conjugate self-assembly. J Mater Sci Technol 114:222–232. https://doi.org/10.1016/j.jmst.2021.10.030

34. Wang W, Li X, Deng F et al (2022) Novel organic/inorganic PDI-Urea/BiOBr S-scheme heterojunction for improved photocatalytic antibiotic degradation and H$_2$O$_2$ production. Chin Chem Lett. https://doi.org/10.1016/j.cclet.2022.01.058

35. Li X, Liu Q, Deng F et al (2022) Double-defect-induced polarization enhanced OV-BiOBr/Cu$_{2-x}$S high-low junction for boosted photoelectrochemical hydrogen evolution. Appl Catal B 314:121502. https://doi.org/10.1016/j.apcatb.2022.121502

36. Long Y, Li L, Zhou L (2020) Fabrication of the AgI/BiOI/BiPO$_4$ multi-heterojunction with high photocatalytic activity. Mater Res Bull 126:110787. https://doi.org/10.1016/j.materresbull.2020.110787

37. Yan Q, Xie X, Liu Y et al (2019) Constructing a new Z-scheme multi-heterojunction photocataslyts Ag–AgI/BiOI-Bi$_2$O$_3$ with enhanced photocatalytic activity. J Hazard Mater 371:304–315. https://doi.org/10.1016/j.jhazmat.2019.03.031

38. Wang K, Qian Z, Guo W (2019) Multi-heterojunction of SnO$_2$/Bi$_2$O$_3$/BiOI nanofibers: facile fabrication with enhanced visible-light photocatalytic performance. Mater Res Bull 111:202–211. https://doi.org/10.1016/j.materresbull.2018.11.005

39. Huang Y, Fan W, Long B et al (2016) Visible light Bi$_2$S$_3$/Bi$_2$O$_3$/Bi$_2$O$_2$CO$_3$ photocatalyst for effective degradation of organic pollutions. Appl Catal B 185:68–76. https://doi.org/10.1016/j.apcatb.2015.11.043

40. Zhou Y, Wang H, Sheng M et al (2013) Environmentally friendly room temperature synthesis and humidity sensing applications of nanostructured Bi$_2$O$_2$CO$_3$. Sens Actuators B Chem 188:1312–1318. https://doi.org/10.1016/j.snb.2013.08.041

41. Dong F, Lee SC, Wu Z et al (2011) Rose-like monodisperse bismuth subcarbonate hierarchical hollow microspheres: one-pot template-free fabrication and excellent visible light photocatalytic activity and photochemical stability for NO removal in indoor air. J Hazard Mater 195:346–354. https://doi.org/10.1016/j.jhazmat.2011.08.050

42. Dong F, Sun Y, Fu M et al (2012) Novel in situ N-doped (BiO)$_2$CO$_3$ hierarchical microspheres self-assembled by nanosheets as efficient and durable visible light driven photocatalyst. Langmuir 28:766–773. https://doi.org/10.1021/la202752q

43. Wang P, Xu L, Ao Y, Wang C (2017) In-situ growth of Au and β-Bi$_2$O$_3$ nanoparticles on flower-like Bi$_2$O$_2$CO$_3$: a multi-heterojunction photocatalyst with enhanced visible light responsive photocatalytic activity. J Colloid Interface Sci 495:122–129. https://doi.org/10.1016/j.jcis.2017.02.003

44. Nuñez-Briones A, García-Cerda L, Rodríguez-Hernández J et al (2018) Synthesis, structural characterization, and photocatalytic activity of Bi-based nanoparticles. Int J Appl Ceram Technol 15:101–110. https://doi.org/10.1111/ijac.12765

45. Wang W, Cheng H, Huang B et al (2013) Synthesis of Bi$_2$O$_2$CO$_3$/Bi$_2$S$_3$ hierarchical microspheres with heterojunctions and their enhanced visible light-driven photocatalytic degradation of dye pollutants. J Colloid Interface Sci 402:34–39. https://doi.org/10.1016/j.jcis.2013.03.054

46. Zhao Z, Hao Y, Song X, Deng Z (2020) High visible-light rhodamine B degradation activity over two-dimensional Bi$_2$O$_2$CO$_3$/BiOCl heterojunction through the cohesive and efficient electronic transmission channel. J Mater Sci Mater Electron 31:6726–6734. https://doi.org/10.1007/s10854-020-03229-6

47. Dong F, Ho W-K, Lee SC et al (2011) Template-free fabrication and growth mechanism of uniform (BiO)$_2$CO$_3$ hierarchical hollow microspheres with outstanding photocatalytic activities under both UV and visible light irradiation. J Mater Chem 21:12428. https://doi.org/10.1039/c1jm11840d

48. Sun J, Wang J, Li Z et al (2015) Assembly and electrochemical properties of novel alkaline rechargeable Ni/Bi battery using Ni(OH)$_2$ and (BiO)$_4$CO$_3$(OH)$_2$ microspheres as electrode materials. J Power Sources 274:1070–1075. https://doi.org/10.1016/j.jpowsour.2014.10.172

49. Dong Y, Ma A, Zhang D et al (2020) Preparation of high-performance α-Bi$_2$O$_3$ photocatalysts and their photocatalytic activity. Surf Innov 8:295–303. https://doi.org/10.1680/jsuin.20.00013

50. Dadashi S, Poursalehi R, Delavari HH (2018) Formation, gradual oxidation mechanism and tunable optical properties of Bi/Bi$_2$O$_3$ nanoparticles prepared by Nd:YAG laser ablation in liquid: dissolved oxygen as genesis of tractable oxidation. Mater Res Bull 97:421–427. https://doi.org/10.1016/j.materresbull.2017.09.029

51. Sun D, Huang L, Li L et al (2020) Plasma enhanced Bi/Bi$_2$O$_2$CO$_3$ heterojunction photocatalyst via a novel in-situ method. J Colloid Interface Sci 571:80–89. https://doi.org/10.1016/j.jcis.2020.03.021

52. Yu C, Zhou W, Zhu L et al (2016) Integrating plasmonic Au nanorods with dendritic like α-Bi$_2$O$_3$/Bi$_2$O$_2$CO$_3$ heterostructures for superior visible-light-driven photocatalysis. Appl Catal B 184:1–11. https://doi.org/10.1016/j.apcatb.2015.11.026

53. Hashemi E, Poursalehi R, Delavari H (2019) Formation mechanisms, structural and optical properties of Bi/Bi$_2$O$_3$ One dimensional nanostructures prepared via oriented aggregation of bismuth based nanoparticles synthesized by DC arc discharge in water. Mater Sci Semicond Process 89:51–58. https://doi.org/10.1016/j.mssp.2018.08.028

54. Hashemi E, Poursalehi R, Delavari H (2022) A comparative study of the effects of phase composition on optical properties and photocatalytic activity of α-/β-/γ-Bi$_2$O$_3$ multi-heterojunction prepared by submerged DC electrical arc discharge. Mater Technol. https://doi.org/10.1080/10667857.2022.2037306

55. Ziashahabi A, Prato M, Dang Z et al (2019) The effect of silver oxidation on the photocatalytic activity of Ag/ZnO hybrid plasmonic/metal-oxide nanostructures under visible light and in the dark. Sci Rep 9:11839. https://doi.org/10.1038/s41598-019-48075-7

56. Farajimotlagh M, Poursalehi R, Aliofkhazraei M (2017) Synthesis mechanisms, optical and structural properties of η-Al$_2$O$_3$ based nanoparticles prepared by DC arc discharge in environmentally friendly liquids. Ceram Int 43:7717–7723. https://doi.org/10.1016/j.ceramint.2017.03.075

57. Rahnemai Haghighi N, Poursalehi R (2019) Effect of C/H and C/O ratios on the arc discharge synthesis of titanium carbide nanoparticles in organic liquids. Appl Nanosci. https://doi.org/10.1007/s13204-018-00946-7

58. Hashemi E, Poursalehi R, Delavari H (2022) Shed light on the effect of carrier organic liquids on size, phase composition and optical properties of colloidal bismuth nanoparticles prepared by submerged DC electrical arc discharge. J Mater Res. https://doi.org/10.1557/s43578-022-00636-9

59. Delaportas D, Svarnas P, Alexandrou I et al (2009) γ-Al$_2$O$_3$ nanoparticle production by arc-discharge in water: in situ discharge characterization and nanoparticle investigation. J Phys D Appl Phys 42:245204. https://doi.org/10.1088/0022-3727/42/24/245204

60. Wang Q, Zhang C, Wu H et al (2019) Fabrication of β-phase AgI and Bi$_2$O$_3$ co-decorated Bi$_2$O$_2$CO$_3$ heterojunctions with enhanced photocatalytic performance. J Colloid Interface Sci 547:1–13. https://doi.org/10.1016/j.jcis.2019.03.088

61. Le VH, Nguyen TH, Nguyen HH et al (2020) Fabrication and electrochemical behavior investigation of a Pt-loaded reduced graphene oxide composite (Pt@rGO) as a high-performance cathode for dye-sensitized solar cells. Int J Photoenergy 2020:1–10. https://doi.org/10.1155/2020/8927124

62. Bulmahn JC, Tikhonowski G, Popov AA et al (2020) Laser-ablative synthesis of stable aqueous solutions of elemental bismuth nanoparticles for multimodal theranostic applications. Nanomaterials 10:1463. https://doi.org/10.3390/nano10081463

63. Lamia Bourj Study of CeO$_2$–Bi$_2$O$_3$ system for catalyst and conductivity applications. Autre. Université de Toulon; Université Ibn Zohr (Agadir, Maroc). Faculté des sciences

64. Taylor P, Sunde S, Lopata VJ (1984) Structure, spectra, and stability of solid bismuth carbonates. Can J Chem 62:2863–2873

65. Greaves C, Blower SK (1988) Structural relationships between Bi$_2$O$_2$CO$_3$ and β-Bi$_2$O$_3$. Mater Res Bull 23:1001–1008. https://doi.org/10.1016/0025-5408(88)90055-4

66. Zhou L, Wang W, Xu H et al (2009) Bi$_2$O$_3$ hierarchical nanostructures: controllable synthesis, growth mechanism, and their application in photocatalysis. Chem Eur J 15:1776–1782. https://doi.org/10.1002/chem.200801234

67. Zhang L, Wang W, Zhou L, Xu H (2007) Bi$_2$WO$_6$ nano- and microstructures: shape control and associated visible-light-driven photocatalytic activities. Small 3:1618–1625. https://doi.org/10.1002/smll.200700043

68. Yu J, Xiong J, Cheng B, Liu S (2005) Fabrication and characterization of Ag–TiO$_2$ multiphase nanocomposite thin films with enhanced photocatalytic activity. Appl Catal B 60:211–221. https://doi.org/10.1016/j.apcatb.2005.03.009

69. Tilaki RM, Irajizad A, Mahdavi SM (2006) Stability, size and optical properties of silver nanoparticles prepared by laser ablation in different carrier media. Appl Phys A 84:215–219. https://doi.org/10.1007/s00339-006-3604-2

70. Ziashahabi A, Poursalehi R, Naseri N (2018) Shed light on submerged DC arc discharge synthesis of low band gap gray Zn/ZnO nanoparticles: formation and gradual oxidation mechanism. Adv Powder Technol 29:1246–1254. https://doi.org/10.1016/j.apt.2018.02.017

71. Vasanthkumar K, Porkodi K, Selvaganapathi A (2007) Constrain in solving Langmuir-Hinshelwood kinetic expression for the photocatalytic degradation of Auramine O aqueous solutions by ZnO catalyst. Dyes Pigm 75:246–249. https://doi.org/10.1016/j.dyepig.2006.05.035

72. Iyyapushpam S, Nishanthi ST, Pathinettam Padiyan D (2012) Synthesis of room temperature bismuth oxide and its photocatalytic activity. Mater Lett 86:25–27. https://doi.org/10.1016/j.matlet.2012.07.015

73. Yu C, Liu X, Liu R et al (2020) Hierarchical BiOHC$_2$O$_4$/Bi$_2$O$_2$CO$_3$ composite microrods fabricated via insitu anion ion-exchange and their advanced photocatalytic performance. J Alloy Compd 840:155687. https://doi.org/10.1016/j.jallcom.2020.155687

74. Li Y, Zhang Z, Zhang Y et al (2014) Preparation of Ag doped Bi$_2$O$_3$ nanosheets with highly enhanced visible light photocatalytic performances. Ceram Int 40:13275–13280. https://doi.org/10.1016/j.ceramint.2014.05.037

75. Zhou L, Cai M, Zhang X et al (2019) Key role of hydrochar in heterogeneous photocatalytic degradation of sulfamethoxazole using Ag$_3$PO$_4$-based photocatalysts. RSC Adv 9:35636–35645. https://doi.org/10.1039/C9RA07843F

76. Su F, Li P, Huang J et al (2021) Photocatalytic degradation of organic dye and tetracycline by ternary Ag$_2$O/AgBr–CeO$_2$ photocatalyst under visible-light irradiation. Sci Rep 11:85. https://doi.org/10.1038/s41598-020-76997-0

77. Sorathiya K, Mishra B, Kalarikkal A et al (2016) Enhancement in rate of photocatalysis upon catalyst recycling. Sci Rep 6:35075. https://doi.org/10.1038/srep35075

78. Li X, Xiong J, Gao X et al (2020) Novel BP/BiOBr S-scheme nano-heterojunction for enhanced visible-light photocatalytic tetracycline removal and oxygen evolution activity. J Hazard Mater 387:121690. https://doi.org/10.1016/j.jhazmat.2019.121690

79. Xiong J, Li X, Huang J et al (2020) CN/rGO@BPQDs high-low junctions with stretching spatial charge separation ability for photocatalytic degradation and H2O2 production. Appl Catal B 266:118602. https://doi.org/10.1016/j.apcatb.2020.118602

80. Li X, Liu J, Huang J et al (2020) All organic S-scheme heterojunction PDI-Ala/S-C$_3$N$_4$ photocatalyst with enhanced photocatalytic performance. Acta Phys Chim Sin. https://doi.org/10.3866/PKU.WHXB202010030

81. Zahid AH, Han Q (2021) A review on the preparation, microstructure, and photocatalytic performance of Bi$_2$O$_3$ in polymorphs. Nanoscale 13:17687–17724. https://doi.org/10.1039/D1NR03187B

82. Kong S, An Z, Zhang W et al (2019) Preparation of hollow flower-like microspherical β-Bi$_2$O$_3$/BiOCl heterojunction and high photocatalytic property for tetracycline hydrochloride degradation. Nanomaterials 10:57. https://doi.org/10.3390/nano10010057

83. Liu W, Zhou J, Zhou J (2019) Facile fabrication of multi-walled carbon nanotubes (MWCNTs)/α-Bi$_2$O$_3$ nanosheets composite with enhanced photocatalytic activity for doxycycline degradation under visible light irradiation. J Mater Sci 54:3294–3308. https://doi.org/10.1007/s10853-018-3090-x

84. Li H, Hu T, Zhang R et al (2016) Preparation of solid-state Z-scheme Bi$_2$MoO$_6$/MO (M Cu, Co 3/4, or Ni) heterojunctions with internal electric field-improved performance in photocatalysis. Appl Catal B 188:313–323. https://doi.org/10.1016/j.apcatb.2016.02.015

Publisher's Note